Inorganic Chemistry

pubs.acs.org/IC Article

3d-4f Resonant Inelastic X-ray Scattering of Actinide Dioxides: Crystal-Field Multiplet Description

Sergei M. Butorin*

Cite This: *Inorg. Chem.* 2020, 59, 16251−16264

Read Online

ACCESS | Metrics & More | Article Recommendations

ABSTRACT: A theoretical overview of the core-to-core (3*d*-4*f*) resonant inelastic X-ray scattering (RIXS) spectra of actinide dioxides AnO_2 (An = Th, U, Np, Pu, Am, Cu, Bk, Cf) is provided. The 3*d*-4*f* RIXS maps were calculated using crystal-field multiplet theory and turned out to be significantly different at the An M_5 vs M_4 edges, because of selection rules and final state effects. The results of the calculations allowed for a general analysis of so-called high-energy-resolution fluorescence-detected X-ray absorption (HERFD-XAS) spectra. The cuts of the calculated RIXS maps along the incident energy axis at the constant emitted energy, corresponding to the maximum of the RIXS intensity, represented the HERFD spectra and provided their comparison with calculated conventional X-ray absorption (XAS) spectra with a reduced core-hole lifetime broadening at the An M_5 and M_4 edges. Although the An M_5 HERFD profiles were found to depart from the X-ray absorption cross-section, in terms of appearing additional transitions, the results of calculations for the An M_4 edges demonstrate overall better agreement between the HERFD and XAS spectra for most dioxides, keeping in mind a restricted HERFD resolution, because of the core−hole lifetime broadening in the final state. The results confirm the utility of HERFD for the An chemical state determination and indicate the importance of calculating the entire RIXS process in order to interpret the HERFD data correctly.

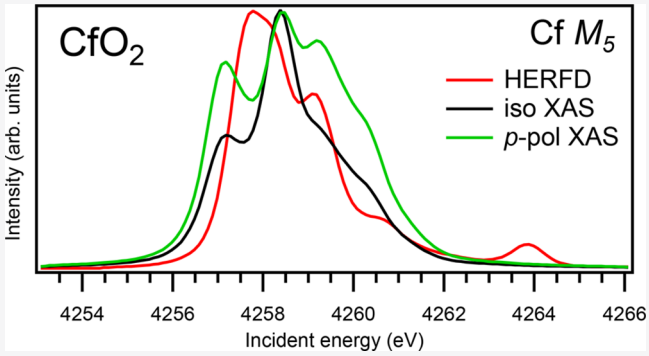

INTRODUCTION

The application of the high-energy-resolution fluorescence detected X-ray absorption (HERFD-XAS) technique to actinide (An) compounds has led to a striking improvement in the resolution of the spectra at the An $M_{4,5}$ edges (4−8 times higher, according to various estimates), because of a reduced core−hole lifetime broadening in the final state of the spectroscopic process.[1−3] This can be viewed as a real breakthrough in actinide research, since the enhanced sensitivity of the method allows for probing the An oxidation state, 5*f* occupancy, local symmetry, (non)stoichiometry, oxygen/metal (O/M) ratio, etc. with much greater capability and efficiency. For example, the long-standing questions, such as about the oxidation path from U(IV) to U(VI) in the U−O system[1,4] and possible oxidation of PuO_2 to Pu(V) (see ref 5) were successfully addressed after the employment of the HERFD-XAS technique.

However, in the light of an increasing usage of this technique by scientists involved in the actinide research, the question about how well the profiles of the HERFD-XAS spectra at the An $M_{4,5}$ edges follow the X-ray absorption cross-section becomes important. This is crucial for the interpretation of recorded data with help of spectra of reference systems and/or model calculations. For example, if the HERFD-XAS spectra follow the X-ray absorption cross-section, the calculations of these spectra can be greatly simplified by just calculating the An $M_{4,5}$ XAS with a significantly reduced broadening, instead of calculating the full-path core-to-core (3*d*-to-4*f*) RIXS process with transitions from the ground state to the intermediate states with a 3*d* hole and then to final states with a 4*f* hole.[3,6,7]

This question is especially important for the case when states with a significant degree of localization in the valence and conduction bands are involved in the spectroscopic process (in our case, 5*f* states), i.e., when the multiplet approach is appropriate. For example, Tanaka et al.[8] found some differences between the calculated Dy(III) L_3 XAS spectrum with a reduced core-hole lifetime broadening and the calculated HERFD-XAS spectrum for the region of quadrupole 2*p*−4*f* transitions. Moreover, the X-ray fluorescence yield spectra at the $L_{2,3}$ edges of 3*d* transition metal systems were shown to depart from the X-ray absorption cross-section.[9]

The paper presents the results of the calculations using the crystal-field multiplet theory, which address the questions about

Received: July 9, 2020
Published: November 2, 2020

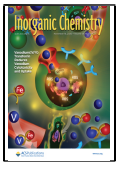

https://dx.doi.org/10.1021/acs.inorgchem.0c02032
Inorg. Chem. 2020, 59, 16251−16264

Table 1. Ab Initio Hartree−Fock Values of Slater Integrals and Spin-Orbit Coupling Constants in the Ground-State Configurations[a]

		Hartree−Fock Values (eV)			
	n	$F^2(5f,5f)$	$F^4(5f,5f)$	$F^6(5f,5f)$	$\zeta(5f)$
Th(IV)	0	0	0	0	0
U(IV)	2	9.514	6.224	4.569	0.261
Np(IV)	3	9.907	6.489	4.767	0.297
Pu(IV)	4	10.282	6.741	4.955	0.334
Am(IV)	5	10.642	6.982	5.136	0.373
Cm(IV)	6	10.990	7.216	5.310	0.414
Bk(IV)	7	11.328	7.442	5.479	0.457
Cf(IV)	8	11.657	7.662	5.642	0.502

[a]In the RIXS calculation, the Slater integrals were reduced to 80% of these values.

the relationship between HERFD and conventional XAS spectra. The choice to apply these calculations to systems such as An dioxides is understandable, because An dioxides are the most commonly used materials in the nuclear industry. Mixed An dioxides are considered to be good candidates for innovative fuels in Generation IV reactors to recycle major actinides, such as U and Pu, and reduce the radioactive waste by partitioning and transmutating the minor ones, such as Np, Am, and Cm. For the optimized fuel performance, handling, and storage, it is important to gain insight on the An chemical state and cation charge distribution and on the oxygen/metal (O/M) ratio as key parameters to assess thermodynamic, chemical, and physical properties of the fuels. Furthermore, mixed-oxide systems cannot be fully understood without a thorough understanding of each binary oxides in the mix. Advanced X-ray spectroscopic tools, such as HERFD-XAS, with enhanced sensitivity help to link the changes in the electronic structure to specific macroscopic properties of the materials in question.

COMPUTATIONAL DETAILS

The crystal (ligand)-field multiplet approach was used in the calculations, which included the 5*f* and core 3*d* and 4*f* states on a single An ion in cubic symmetry.

The total Hamiltonian of a system can be written as

$$H = H_{\mathrm{FI}} + H_{\mathrm{CF}} \tag{1}$$

where H_{FI} represents the Coulomb, exchange, and spin−orbit interactions for a free actinide ion and H_{CF} describes the crystal-field splittings.

$$\begin{aligned} H_{\mathrm{FI}} = & \sum_{\gamma_1,\gamma_2,\gamma_3,\gamma_4} R_{\mathrm{ff}}(\gamma_1,\gamma_2,\gamma_3,\gamma_4) a_{\mathrm{f}}^{\dagger}(\gamma_1) a_{\mathrm{f}}^{\dagger}(\gamma_2) a_{\mathrm{f}}(\gamma_3) a_{\mathrm{f}}(\gamma_4) \\ & + \sum_{\gamma_1,\gamma_2,\mu_1,\mu_2} R_{\mathrm{fd}}(\gamma_1,\mu_1,\mu_2,\gamma_2) a_{\mathrm{f}}^{\dagger}(\gamma_1) a_{\mathrm{d}}^{\dagger}(\mu_1) a_{\mathrm{d}}(\mu_2) a_{\mathrm{f}}(\gamma_2) \\ & + \sum_{\gamma_1,\gamma_2,\lambda_1,\lambda_2} R_{\mathrm{fc}}(\gamma_1,\mu_1,\mu_2,\gamma_2) a_{\mathrm{f}}^{\dagger}(\gamma_1) a_{\mathrm{c}}^{\dagger}(\lambda_1) a_{\mathrm{c}}(\lambda_2) a_{\mathrm{f}}(\gamma_2) \\ & + \zeta(5f) \sum_{\gamma_1,\gamma_2} h_{\gamma_1,\gamma_2} a_{\mathrm{f}}^{\dagger}(\gamma_1) a_{\mathrm{f}}(\gamma_2) + \zeta(3d) \sum_{\mu_1,\mu_2} l_{\mu_1,\mu_2} a_{\mathrm{d}}^{\dagger}(\mu_1) a_{\mathrm{d}}(\mu_2) \\ & + \zeta(4f) \sum_{\lambda_1,\lambda_2} p_{\lambda_1,\lambda_2} a_{\mathrm{c}}^{\dagger}(\lambda_1) a_{\mathrm{c}}(\lambda_2) \end{aligned} \tag{2}$$

where the interaction between 5*f* electrons (R_{ff}) and between a 5*f* electron and a core 3*d* hole (R_{fd}) or a core 4*f* hole (R_{fc}) is described in terms of Slater integrals, while the spin−orbit interaction for the 5*f* and core 3*d* or 4*f* states is described with coupling constants $\zeta(5f)$, $\zeta(3d)$ and $\zeta(4f)$, respectively, and matrix elements *h*, *l*, and *p* of the spin−orbit coupling operator. $a^{\dagger}$ is an electron creation operator and γ, μ, and λ are combined indices to specify the spin and orbital degeneracies of 5*f*, 3*d*, and 4*f* states, respectively.

$$H_{\mathrm{CF}} = \sum_{\gamma,\gamma'} Q^{\mathrm{CF}}_{\gamma\gamma'} a_{\mathrm{f}}^{\dagger}(\gamma) a_{\mathrm{f}}(\gamma') \tag{3}$$

where Q^{CF} is the potential provided by the crystal environment around the actinide ion, which can be expanded, in terms of tensor operators C_q^k, as

$$Q^{\mathrm{CF}} = \sum_{k,q} B_q^k C_q^k \tag{4}$$

where B_q^k are Wybourne's crystal-field parameters. The C_q^k are related to the spherical harmonics as

$$C_q^k = \sqrt{\frac{4\pi}{2k+1}}\, Y_q^k \tag{5}$$

For *f* electrons, the terms in the expansion with $k \leq 6$ are nonzero. For cubic site symmetry as in actinide dioxides, only two crystal field parameters (one of rank 4 and one of rank 6) are independent. The crystal field potential can be rewritten as

$$Q^{\mathrm{CF}} = B_0^4\left[C_0^4 + \sqrt{\frac{5}{14}}\,(C_4^4 + C_{-4}^4)\right] + B_0^6\left[C_0^6 - \sqrt{\frac{7}{2}}\,(C_4^6 + C_{-4}^6)\right] \tag{6}$$

To calculate the An HERFD spectra at the M_4 ($3d_{3/2} \rightarrow 5f_{5/2},7p$) transitions) and M_5 ($3d_{5/2} \rightarrow 5f_{7/2,5/2}$ transitions) edges, the core-to-core (3*d*-to-4*f*) RIXS maps around the An *Mβ* ($4f_{5/2} \rightarrow 3d_{3/2}$

Table 2. Ab Initio Hartree-Fock Values of Slater Integrals and Spin-Orbit Coupling Constants in the Intermediate-State Configurations[a]

	Hartree−Fock Values (eV)									
	$F^2(5f,5f)$	$F^4(5f,5f)$	$F^6(5f,5f)$	$\zeta(5f)$	$F^2(3d,5f)$	$F^4(3d,5f)$	$G^1(3d,5f)$	$G^3(3d,5f)$	$G^5(3d,5f)$	$\zeta(3d)$
Th(IV)	0	0	0	0.233	2.192	1.008	1.694	1.022	0.714	66.004
U(IV)	10.025	6.572	4.831	0.301	2.564	1.190	2.003	1.211	0.847	73.384
Np(IV)	10.394	6.820	5.016	0.338	2.741	1.277	2.151	1.301	0.910	77.308
Pu(IV)	10.750	7.059	5.194	0.377	2.915	1.362	2.296	1.390	0.973	81.395
Am(IV)	11.093	7.289	5.366	0.418	3.085	1.447	2.439	1.478	1.035	85.649
Cm(IV)	11.427	7.512	5.532	0.461	3.251	1.529	2.578	1.563	1.095	90.076
Bk(IV)	11.754	7.731	5.695	0.506	3.410	1.607	2.710	1.645	1.152	94.681
Cf(IV)	12.072	7.943	5.854	0.553	3.568	1.685	2.844	1.727	1.210	99.468

[a]In the RIXS calculation, the Slater integrals were reduced to 80% of these values.

https://dx.doi.org/10.1021/acs.inorgchem.0c02032
Inorg. Chem. 2020, 59, 16251−16264

Table 3. Ab Initio Hartree−Fock Values of Slater Integrals and Spin-Orbit Coupling Constants in the Final-State Configurations[a]

	Hartree−Fock Values (eV)											
	$F^2(5f,5f)$	$F^4(5f,5f)$	$F^6(5f,5f)$	$\zeta(5f)$	$F^2(4f,5f)$	$F^4(4f,5f)$	$F^6(4f,5f)$	$G^0(4f,5f)$	$G^2(4f,5f)$	$G^4(4f,5f)$	$G^6(4f,5f)$	$\zeta(4f)$
Th(IV)	0	0	0	0.227	4.577	1.950	1.200	1.211	1.494	1.161	0.905	2.662
U(IV)	9.963	6.534	4.804	0.294	5.209	2.255	1.394	1.380	1.721	1.343	1.050	3.078
Np(IV)	10.332	6.782	4.989	0.330	5.503	2.398	1.485	1.457	1.826	1.428	1.117	3.302
Pu(IV)	10.687	7.020	5.167	0.368	5.787	2.536	1.573	1.531	1.927	1.509	1.182	3.538
Am(IV)	11.031	7.250	5.339	0.409	6.062	2.670	1.658	1.601	2.024	1.588	1.245	3.785
Cm(IV)	11.365	7.474	5.505	0.451	6.328	2.799	1.740	1.670	2.119	1.665	1.306	4.044
Bk(IV)	11.690	7.691	5.667	0.495	6.588	2.926	1.821	1.736	2.210	1.739	1.365	4.315
Cf(IV)	12.008	7.903	5.826	0.542	6.843	3.050	1.900	1.801	2.300	1.813	1.423	4.600

[a]In the RIXS calculation, the Slater integrals were reduced to 80% of these values.

Table 4. Values of Wybourne's Crystal-Field Parameters Used in the RIXS Calculation

parameter	Th(IV)	U(IV)	Np(IV)	Pu(IV)	Am(IV)	Cm(IV)	Bk(IV)	Cf(IV)
B_0^4	−1.30 eV	−0.93 eV	−0.84 eV	−1.21 eV	−0.84 eV	−0.80 eV	−0.80 eV	−0.80 eV
B_0^6	0.55 eV	0.35 eV	0.34 eV	0.50 eV	0.27 eV	0.15 eV	0.15 eV	0.15 eV
ref(s)	3	7, 11	12, 13	14	13, 15	13, 16		

transitions) and An $M\alpha$ ($4f_{7/2,5/2} \rightarrow 3d_{5/2}$ transitions) X-ray emission lines were calculated. In terms of electronic configurations, the $5f^n \rightarrow 3d^9 5f^{n+1} \rightarrow 4f^{13} 5f^{n+1}$ excitation−de-excitation path was used. The transitions to np continuum states were neglected.

The multiplets of the ground state $5f^n$, intermediate state $3d^9 5f^{n+1}$, and final state $4f^{13} 5f^{n+1}$ configurations are defined by spin−orbit, electrostatic (F^k), and exchange G^k) interactions and by applied crystal field. The ab initio values of Slater integrals $F^{2,4,6}(5f,5f)$, $F^{2,4}(3d,5f)$, $F^{2,4,6}(4f,5f)$, $G^{1,3,5}(3d,5f)$, $G^{0,2,4,6}(4f,5f)$ and spin−orbit coupling constants $\zeta(5f)$, $\zeta(3d)$, $\zeta(4f)$ are summarized in Tables 1−3, which are related to the ground, intermediate, and final state configurations, respectively.

In the actual multiplet calculations, the Slater integrals were reduced to 80% of their ab initio atomic values to account for intra-atomic relaxation effects, as well as hybridization effects in solids. There is a certain consensus to apply such a level of the Slater integral reduction for compounds.[10] The values of Wybourne's crystal-field parameters for cubic symmetry B_0^4 and B_0^6 (values for Stevens parameters can be obtained by multiplying with $\frac{1}{8}$ and $\frac{1}{16}$, respectively), which were used in the calculations, are given in Table 4, along with references from where they were adopted. In addition, the direct interatomic exchange and superexchange, treated as a magnetic field along the z-axis and acting on the spin S, was set to 0.001 eV.

The $3d$-to-$4f$ RIXS maps were calculated using the Kramers−Heisenberg formula:

$$I(\omega, \omega') = \sum_j \left| \sum_m \frac{\langle f|D_2|m\rangle\langle m|D_1|g\rangle}{E_g + \omega - E_m - i\Gamma_m/2} \right|^2 \times \frac{\Gamma_f/\pi}{(E_f + \omega' - E_g - \omega)^2 + \Gamma_f^2} \quad (7)$$

where $|g\rangle$, $|m\rangle$ and $|f\rangle$ are the ground, intermediate, and final states of the spectroscopic process with energies E_g, E_m, and E_f, respectively. ω and ω' are the energies of the incident and scattered/emitted photons with polarizations q_1 and q_2, respectively, and Γ_m and Γ_f are the lifetime broadenings of the intermediate and final states, in terms of half width at half-maximum (HWHM) of the Lorentzian function. Operators for optical dipole transitions D are expressed in terms of spherical tensor operators $C_q^{(1)}$. For a transition to the intermediate state:

$$D_1 = \mathbf{e}\cdot\mathbf{r} = r\left[-\frac{1}{\sqrt{2}}(e_x - ie_y)C_1^{(1)} + \frac{1}{\sqrt{2}}(e_x + ie_y)C_{-1}^{(1)} + e_z C_0^{(1)}\right] \quad (8)$$

where $\mathbf{e} = (e_x, e_y, e_z)$ is the polarization vector of a photon and $\mathbf{r}$ is the position operator. For a transition to the final state, D_2 is a Hermite conjugate of D_1 ($D_2 = D_1^\dagger$), which results in a complex conjugate for e. In present RIXS calculations, the 90°-scattering geometry was used, which is usually applied in HERFD experiments. The incident photons were chosen to propagate along the z-axis with linear polarization along the x-axis and parallel to the propagation direction of scattered photons (π-polarized incident photon beam with the polarization vector in the scattering plane). For these settings, the dipole transition operators become

$$D_1 = r\left[-\frac{1}{\sqrt{2}}C_1^{(1)} + \frac{1}{\sqrt{2}}C_{-1}^{(1)}\right] \quad (9)$$

and

$$D_2 = r\left[\frac{i}{\sqrt{2}}C_1^{(1)} + \frac{i}{\sqrt{2}}C_{-1}^{(1)}\right] \quad (10)$$

The HERFD-XAS spectrum is represented by a linear cut of such a RIXS map (see, for example, ref 1) along the diagonal of the plane defined by the incident energy axis and energy transfer axis or parallel to the incident energy axis at a constant emitted energy (the energy of the RIXS intensity maximum in this case) in the plane of the emitted versus incident energies.

The conventional XAS spectra which represent the $5f^n \rightarrow 3d^9 5f^{n+1}$ transitions were calculated using the following equation:

$$I_{XAS}(\omega) = \sum_m |\langle m|D|g\rangle|^2 \frac{\Gamma_m/\pi}{(E_m - E_g - \omega)^2 + \Gamma_m^2} \quad (11)$$

.

https://dx.doi.org/10.1021/acs.inorgchem.0c02032
Inorg. Chem. 2020, 59, 16251−16264

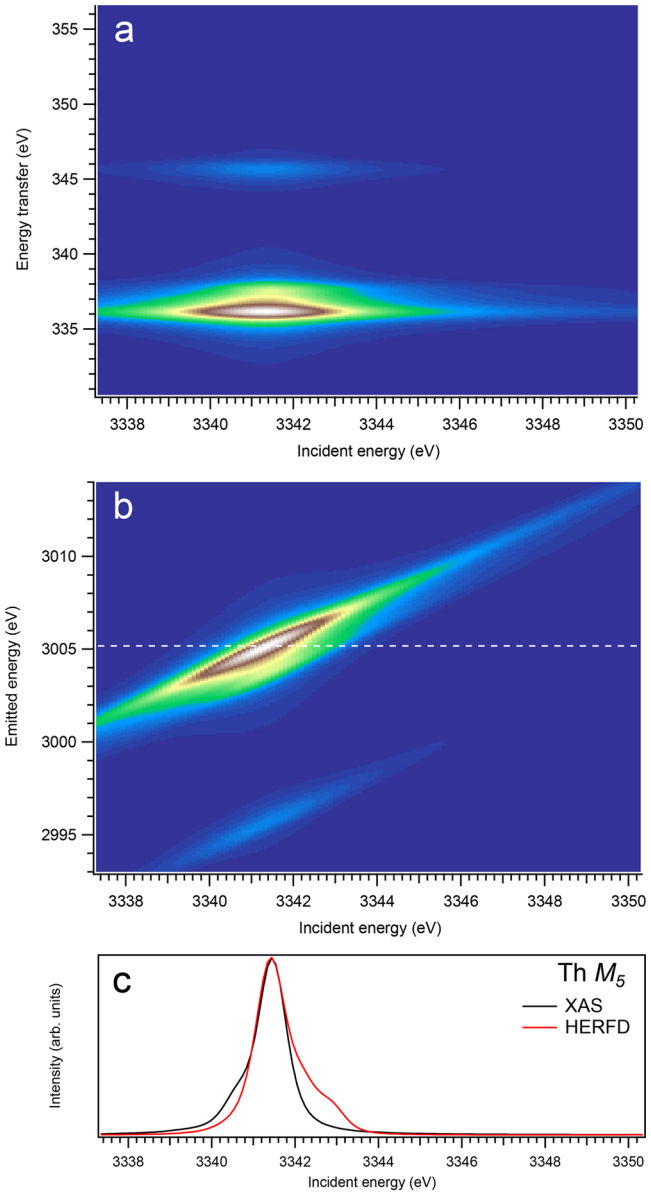

Figure 1. 3*d*-to-4*f* RIXS map of ThO_2 with the incident energy on the *x*-axis and the (a) energy transfer or (b) emitted energy on the *y*-axis. The incident energy varies across the Th M_5 edge. (c) Comparison between the calculated conventional XAS spectrum (black curve) at the Th M_5 edge with a reduced core−hole lifetime broadening and a HERFD cut (red curve) of the 3*d*-to-4*f* RIXS map along the incidence energy axis at an emitted energy corresponding to the RIXS maximum. This cut is indicated by a dashed line in panel (b). The spectra in panel (c) are normalized to a main maximum.

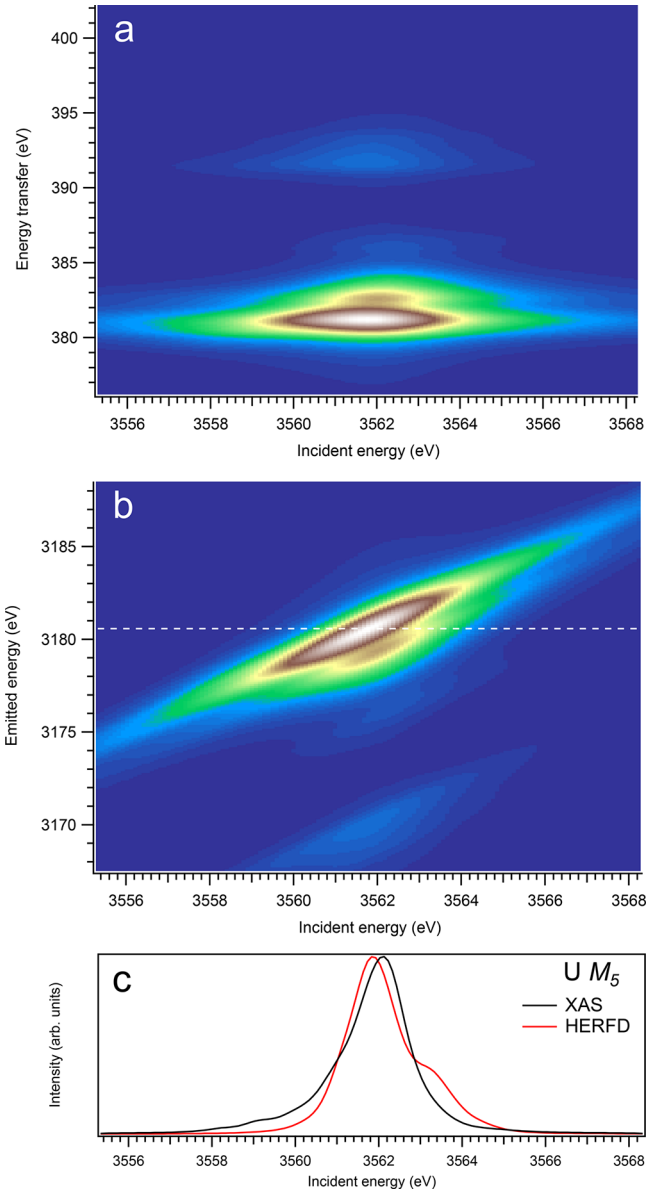

Figure 2. 3*d*-to-4*f* RIXS map of UO_2 with the incident energy on the *x*-axis and the (a) energy transfer or (b) emitted energy on the *y*-axis. The incident energy varies across the U M_5 edge. (c) Comparison between the calculated conventional XAS spectrum (black curve) at the U M_5 edge with a reduced core−hole lifetime broadening and a HERFD cut (red curve) of the 3*d*-to-4*f* RIXS map along the incidence energy axis at an emitted energy corresponding to the RIXS maximum. This cut is indicated by a dashed line in panel (b). The spectra in panel (c) are normalized to a main maximum.

The required Slater integrals F^k, G^k, spin−orbit coupling constants ζ, and transition-matrix elements were obtained with the TT-MULTIPLETS package including Cowan's atomic multiplet program[17] (based on the Hartree−Fock method with relativistic corrections) and Butler's point-group program,[18] which were modified by Thole.[19] In the RIXS calculations, Γ_m and Γ_f were set to values of 1.6 and 0.25 eV, respectively.[20] To simulate the experimental response function, the calculated spectra were additionally broadened with Gaussian with HWHM of 0.25 eV. The conventional XAS spectra are represented by calculated isotropic spectra with the reduced core−hole lifetime broadening (Γ_m = 0.25 eV) and 0.25 eV HWHM Gaussian convolution.

All spectra were calculated for the lowest state of the ground-state configuration. The population of states due to finite temperature was not considered.

RESULTS AND DISCUSSION

Figures 1−8 show the results of the calculations at the An M_5 edges and Figures 9−16 show the results of the calculations at the An M_4 edges. These figures display the 3*d*-to-4*f* RIXS maps by using for the *x*-axis the incident energy scale and, for the *y*-axis, the energy transfer (panel (a)) and emitted energy (panel (b)) scales. Panel (c) makes a comparison between the calculated conventional XAS spectrum at the An M_5 or M_4 edge with a

https://dx.doi.org/10.1021/acs.inorgchem.0c02032
Inorg. Chem. 2020, 59, 16251−16264

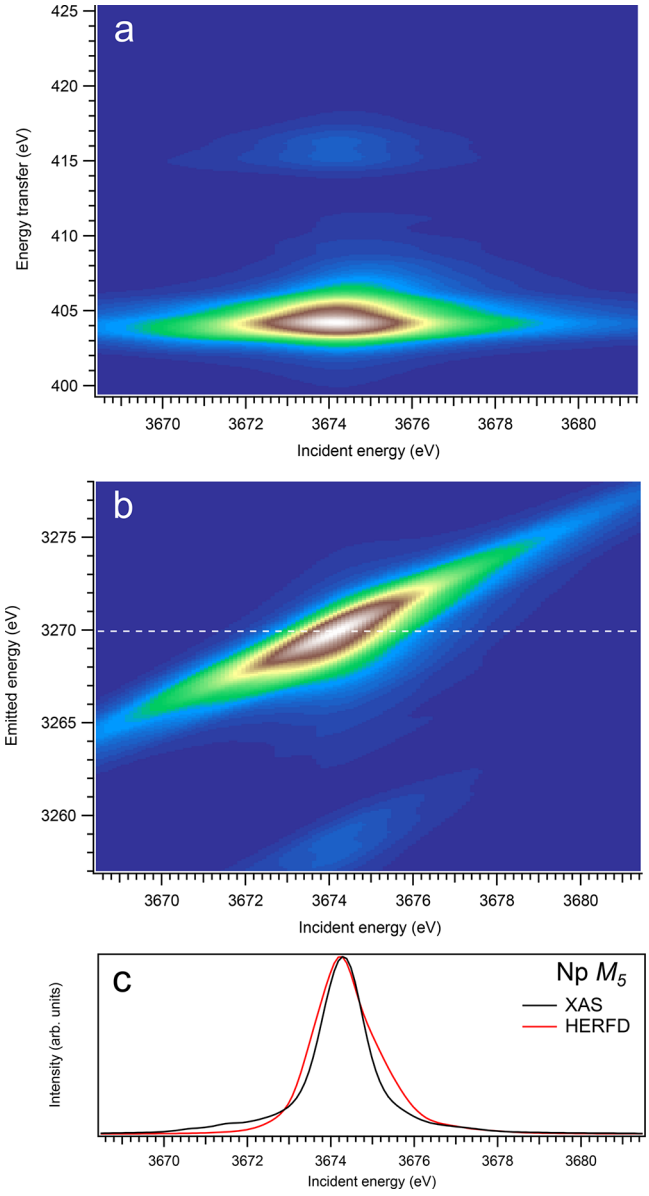

Figure 3. 3*d*-to-4*f* RIXS map of NpO_2 with the incident energy on the *x*-axis and the (a) energy transfer or (b) emitted energy on the *y*-axis. The incident energy varies across the Np M_5 edge. (c) Comparison between the calculated conventional XAS spectrum (black curve) at the Np M_5 edge with a reduced core−hole lifetime broadening and a HERFD cut (red curve) of the 3*d*-to-4*f* RIXS map along the incidence energy axis at an emitted energy corresponding to the RIXS maximum. This cut is indicated by a dashed line in panel (b). The spectra in panel (c) are normalized to a main maximum.

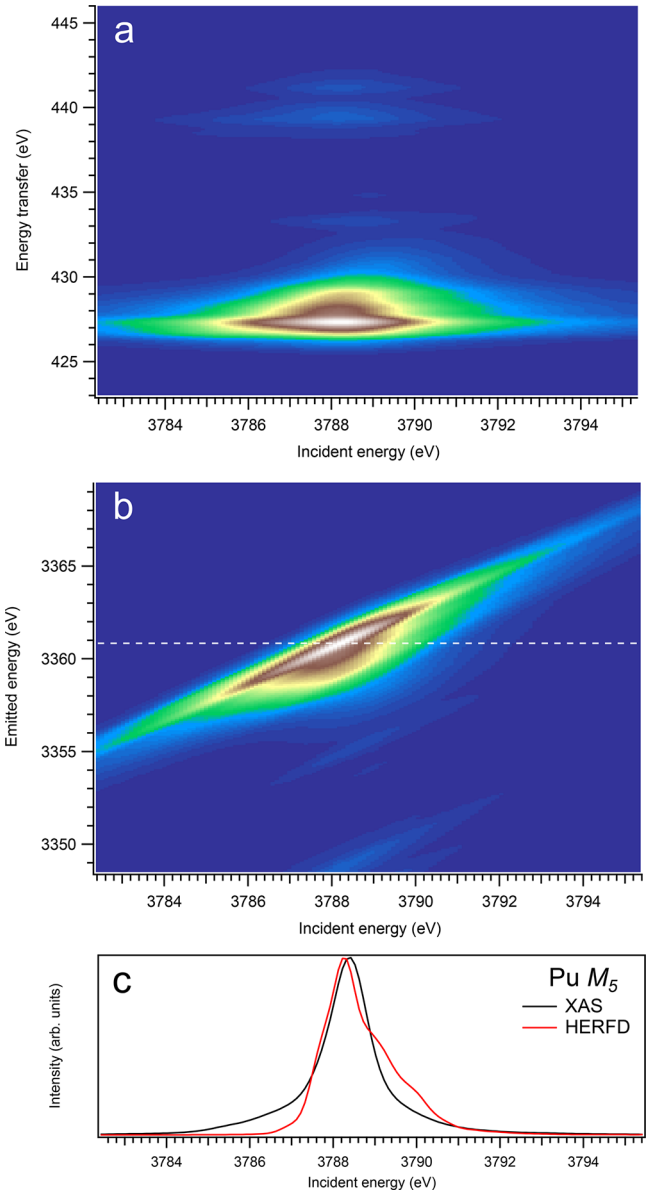

Figure 4. 3*d*-to-4*f* RIXS map of PuO_2 with the incident energy on the *x*-axis and the (a) energy transfer or (b) emitted energy on the *y*-axis. The incident energy varies across the Pu M_5 edge. (c) Comparison between the calculated conventional XAS spectrum (black curve) at the Pu M_5 edge with a reduced core−hole lifetime broadening and a HERFD cut (red curve) of the 3*d*-to-4*f* RIXS map along the incidence energy axis at an emitted energy corresponding to the RIXS maximum. This cut is indicated by a dashed line in panel (b). The spectra in panel (c) are normalized to a main maximum.

reduced core-hole lifetime broadening (0.25 eV HWHM) and a HERFD cut through the 3*d*-to-4*f* RIXS map along the incidence energy axis at an emitted energy corresponding to the RIXS maximum. These cuts are indicated by dashed lines in panel (b) of each figure. In addition, Tables 5 and 6 show the calculated ground state and the energies of lowest 50 states of the ground-state configuration, respectively, for each actinide dioxide.

In contrast to earlier systematic XAS calculations at the *d*-edges of actinides,[21] where only an atomic multiplet approach was used, it is clear that, for the spectra with a significantly improved resolution, the crystal-field interaction must be included in the calculations. This interaction affects the shape of the spectra, as has been already shown[3] for ThO_2, as an example. However, the crystal field influence becomes less pronounced for dioxides of late actinides, because the crystal-field strength is reduced.[13] Other effects may also play a role, such as the increasing relativistic correction and degeneracy lifting of the energy levels with increasing *Z*.

While there are several publications where the crystal field strength in UO_2, NpO_2, and PuO_2 is determined theoretically or from the analysis of various experimental data, much fewer publications related to the crystal field strength in AmO_2 and CmO_2 can be found. To set the values of crystal-field parameters B_0^4 and B_0^6 in our calculations for AmO_2 and CmO_2, a combination of the data for Am(III) and Cm(III), respectively, incorporated into the ThO_2 lattice[15,16] and of the B_0^4 and B_0^6

https://dx.doi.org/10.1021/acs.inorgchem.0c02032
Inorg. Chem. 2020, 59, 16251−16264

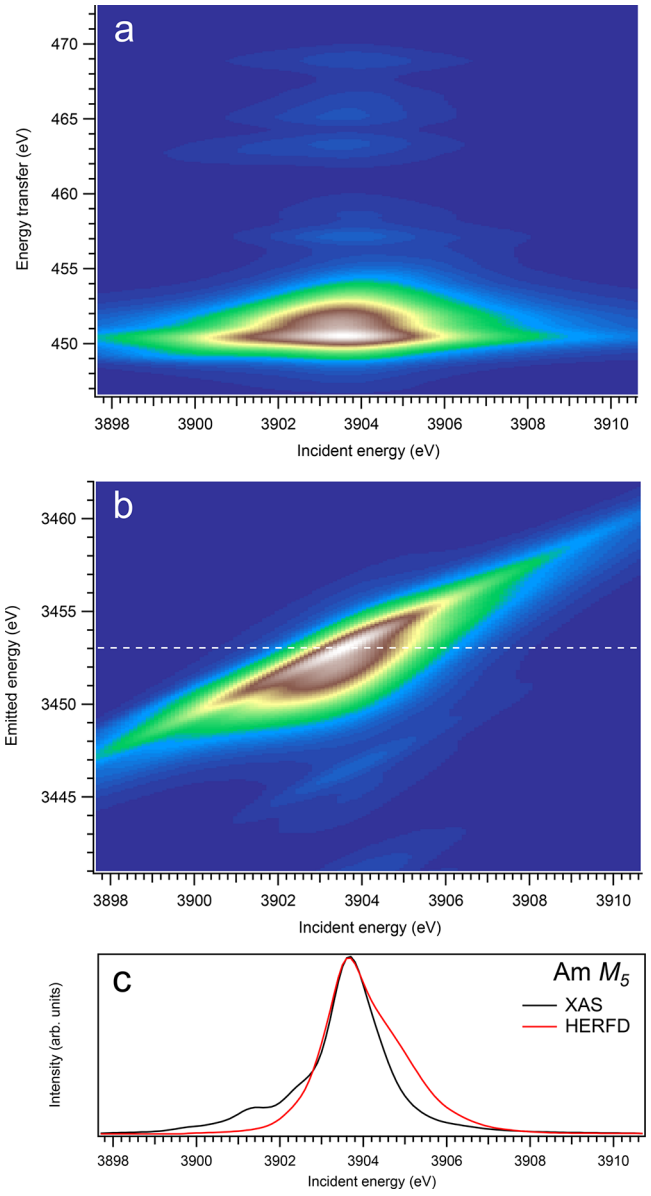

Figure 5. 3*d*-to-4*f* RIXS map of AmO_2 with the incident energy on the *x*-axis and the (a) energy transfer or (b) emitted energy on the *y*-axis. The incident energy varies across the Am M_5 edge. (c) Comparison between the calculated conventional XAS spectrum (black curve) at the Am M_5 edge with a reduced core−hole lifetime broadening and a HERFD cut (red curve) of the 3*d*-to-4*f* RIXS map along the incidence energy axis at an emitted energy corresponding to the RIXS maximum. This cut is indicated by a dashed line in panel (b). The spectra in panel (c) are normalized to a main maximum.

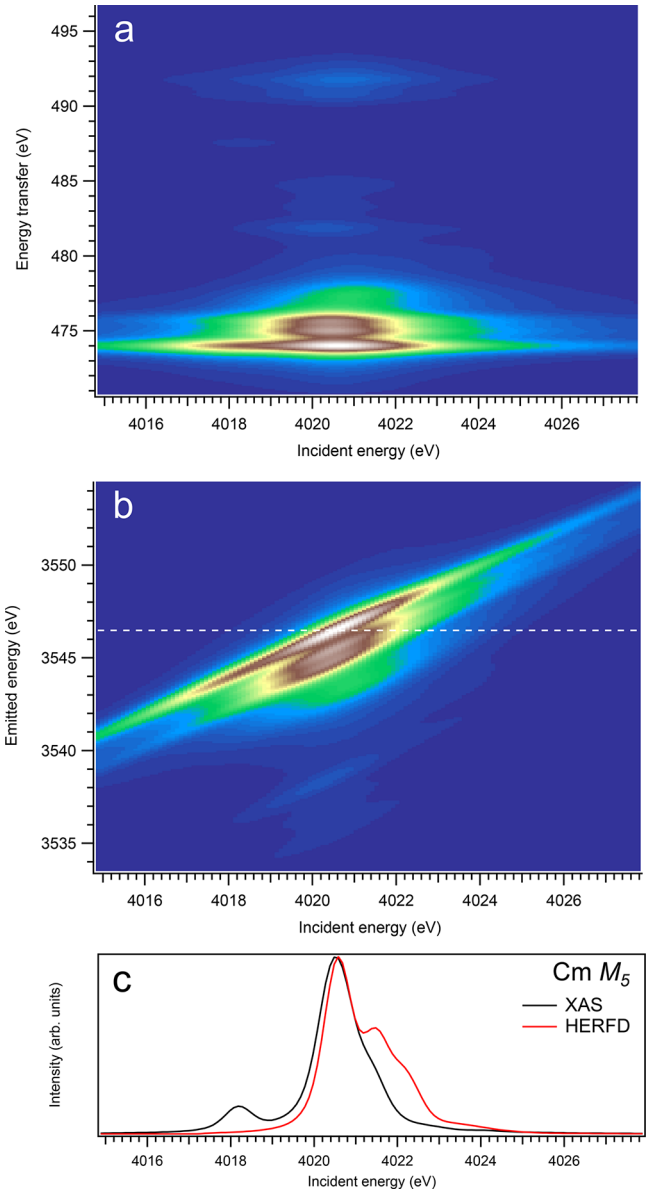

Figure 6. 3*d*-to-4*f* RIXS map of CmO_2 with the incident energy on the *x*-axis and the (a) energy transfer or (b) emitted energy on the *y*-axis. The incident energy varies across the Cm M_5 edge. (c) Comparison between the calculated conventional XAS spectrum (black curve) at the Cm M_5 edge with a reduced core−hole lifetime broadening and a HERFD cut (red curve) of the 3*d*-to-4*f* RIXS map along the incidence energy axis at an emitted energy corresponding to the RIXS maximum. This cut is indicated by a dashed line in panel (b). The spectra in panel (c) are normalized to a main maximum.

estimations within the unified approach for An dioxides, presented in ref 13 was used. We could not find the experimental data related to the crystal-field strength in BkO_2 and CfO_2; therefore, it was decided to use, in the spectral calculations for these dioxides, the same B_0^4 and B_0^6 values as those for CmO_2.

In panel (a) in Figures 1−8, the spectral structures, representing X-ray scattering on the $4f^{13}5f^{n+1}$ multiplet states via virtual $3d^9 5f^{n+1}$ excitations, appear on the constant energy transfer with the varying incident energy throughout the M_5 edge. The energy separation between the intensity maxima of transitions to the $4f^{13}_{7/2}5f^{n+1}$ (associated with $M\alpha_1$) and $4f^{13}_{5/2}5f^{n+1}$ (associated with $M\alpha_2$) components, defined by the 4*f* spin−orbit interaction, gradually increases from ∼9 eV to ∼18 eV when going from ThO_2 to CfO_2.

It has been shown[22−24] for the 3*d* transition-metal (TM) compounds that the constant-incident-energy cut along the energy-transfer axis through the quadrupole part of the 1*s*-2*p* RIXS map of TM, which involves the $1s^1 3d^{n+1}$ excitations, can provide "TM-2*p*-edge-like" information, because the final state configuration includes the $2p^5 3d^{n+1}$ multiplet. In our case, a constant-incident-energy cut through the RIXS maximum in panel (a) in these figures will not represent the XAS spectrum at the An 4*f* edge,[7,25] which includes $4f^{13}6d^1$ multiplet, but rather the $4f \rightarrow 5f$ transition part of the energy-electron-loss (EELS)[26] or nonresonant inelastic X-ray scattering (NIXS)[27] spectra at this edge.

For the An M_4 edges, the 3d-4f RIXS maps (panel (a) in Figures 9−16) appear, overall, to be significantly different from

https://dx.doi.org/10.1021/acs.inorgchem.0c02032
Inorg. Chem. 2020, 59, 16251−16264

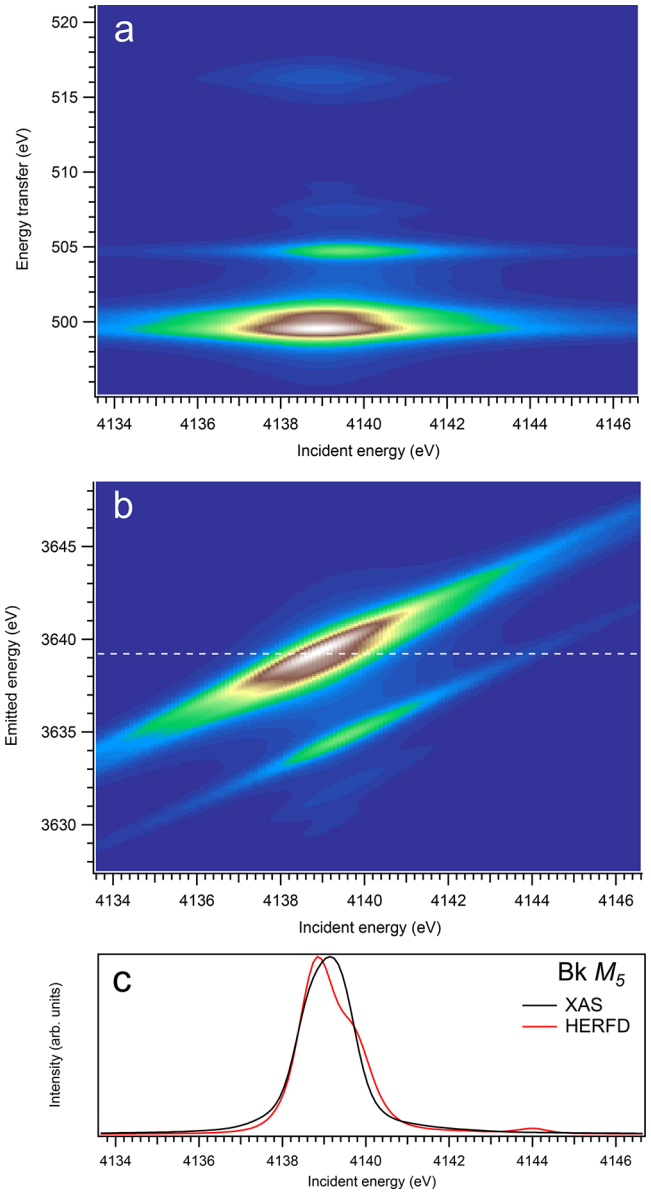

Figure 7. 3*d*-to-4*f* RIXS map of BkO_2 with the incident energy on the *x*-axis and the (a) energy transfer or (b) emitted energy on the *y*-axis. The incident energy varies across the Bk M_5 edge. (c) Comparison between the calculated conventional XAS spectrum (black curve) at the Bk M_5 edge with a reduced core−hole lifetime broadening and a HERFD cut (red curve) of the 3*d*-to-4*f* RIXS map along the incidence energy axis at an emitted energy corresponding to the RIXS maximum. This cut is indicated by a dashed line in panel (b). The spectra in panel (c) are normalized to a main maximum.

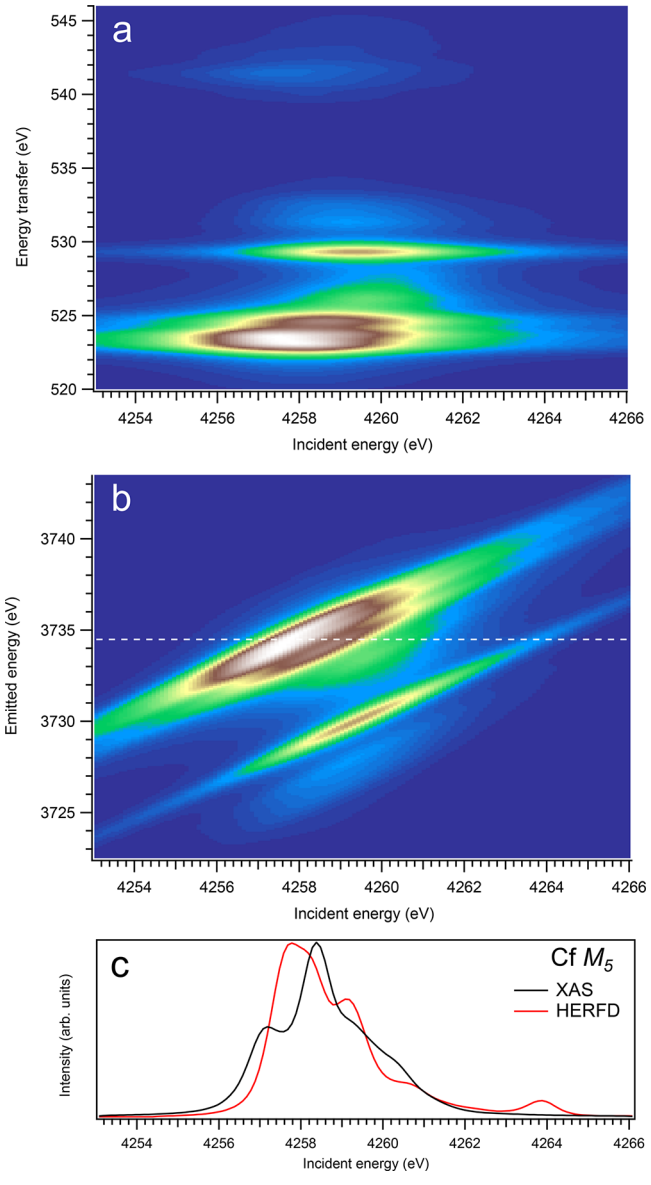

Figure 8. 3*d*-to-4*f* RIXS map of CfO_2 with the incident energy on the *x*-axis and the (a) energy transfer or (b) emitted energy on the *y*-axis. The incident energy varies across the Cf M_5 edge. (c) Comparison between the calculated conventional XAS spectrum (black curve) at the Cf M_5 edge with a reduced core−hole lifetime broadening and a HERFD cut (red curve) of the 3*d*-to-4*f* RIXS map along the incidence energy axis at an emitted energy corresponding to the RIXS maximum. This cut is indicated by a dashed line in panel (b). The spectra in panel (c) are normalized to a main maximum.

those for the An M_5 edges. While no separation into the two transition groups is expected, because of the 4*f* spin−orbit interaction (only the $4f^{13}_{5/2}5f^{n+1}$ multiplet is involved), some calculated (although weak) transitions appear at a quite few eV below and above the main RIXS intensity maximum on the energy-transfer scale. For example, for UO_2 (Figure 10), such transitions can be found at the energy transfer of around 385.9 and 398.8 eV, while the maximum is located at ∼390.5 eV. The ∼385.9 eV and ∼398.8 eV transitions are a result of the interaction of the 4*f* core hole with the 5*f* electrons in the final state of the spectroscopic process and are dependent on the values of exchange integrals $G^k(4f,5f)$.

By plotting the 3*d*-4*f* RIXS map on the emitted energy scale as in panel (b) in Figures 1−16, a connection is made to how the measurements of the HERFD-XAS spectra are performed, when the scattered photons are counted with a X-ray emission spectrometer at a fixed emitted energy while scanning the incident energy across the X-ray absorption edge. Horizontal cuts of the maps in panel (b) in these figures allow one to compare the RIXS profile with the conventional XAS spectrum. Panel (c) in Figures 1−16 provide such a comparison, using a cut through the RIXS intensity maximum (see horizontal white dashed lines in panel (b)), as a representation of the HERFD-XAS spectrum.

At the An M_5 edges of dioxides, for actinides from Th to Cm, a clear trend in differences between calculated conventional XAS

https://dx.doi.org/10.1021/acs.inorgchem.0c02032
Inorg. Chem. 2020, 59, 16251−16264

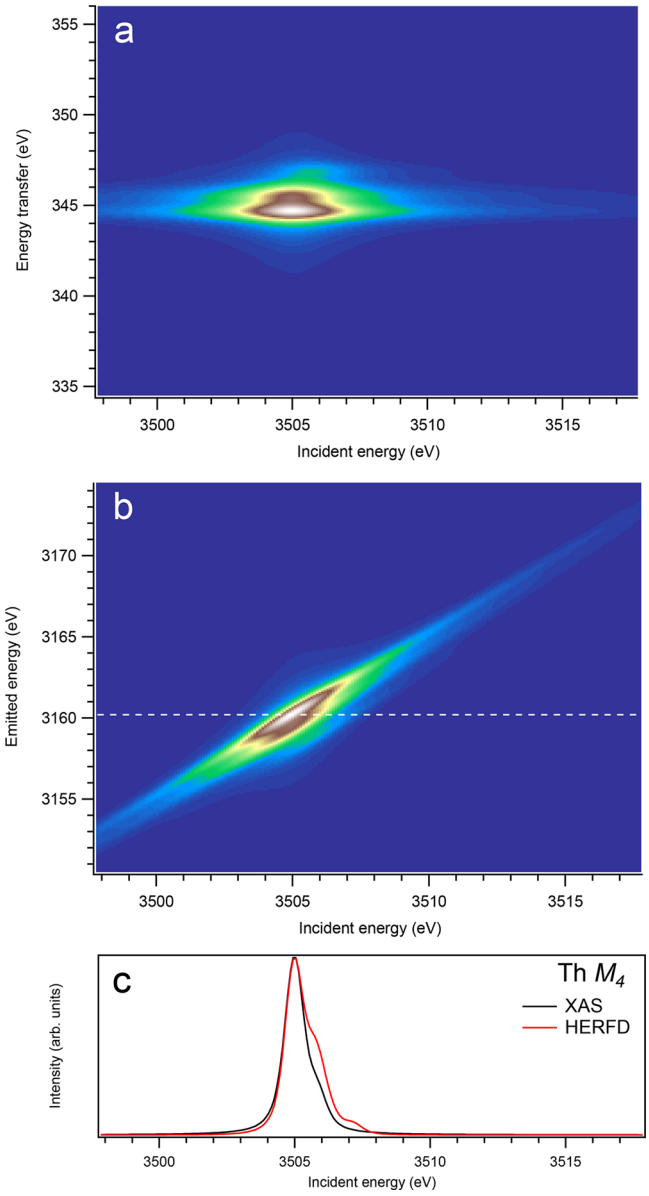

Figure 9. 3*d*-to-4*f* RIXS map of ThO_2 with the incident energy on the *x*-axis and the (a) energy transfer or (b) emitted energy on the *y*-axis. The incident energy varies across the Th M_4 edge. (c) Comparison between the calculated conventional XAS spectrum (black curve) at the Th M_4 edge with a reduced core−hole lifetime broadening and a HERFD cut (red curve) of the 3*d*-to-4*f* RIXS map along the incidence energy axis at an emitted energy corresponding to the RIXS maximum. This cut is indicated by a dashed line in panel (b). The spectra in panel (c) are normalized to a main maximum.

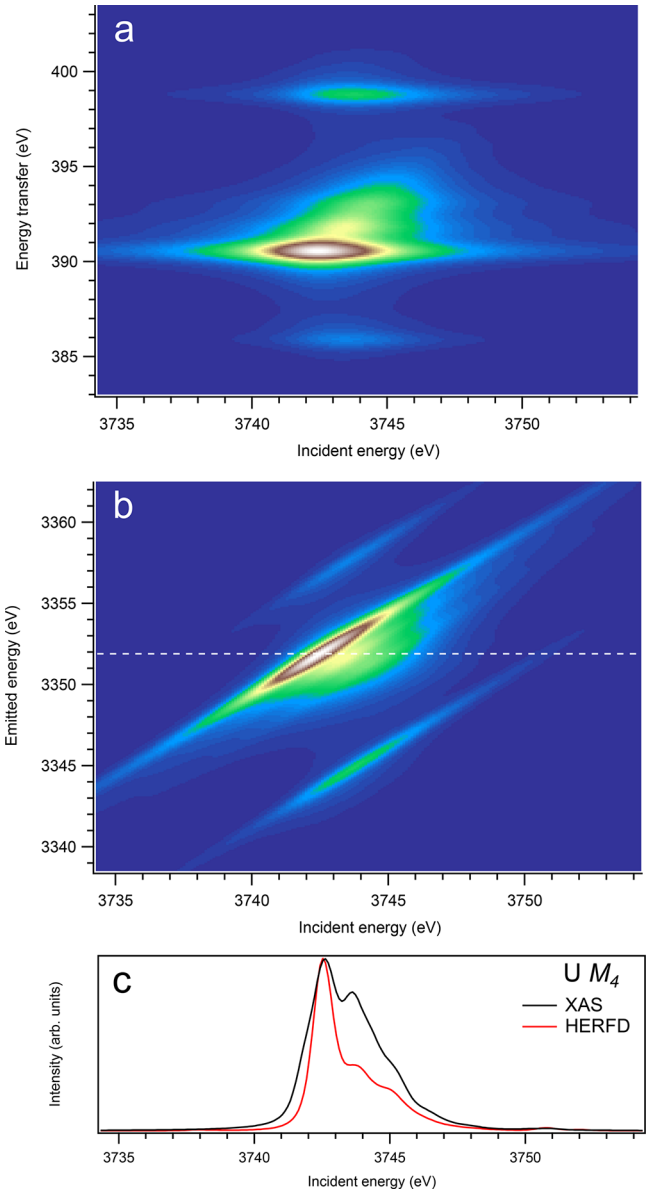

Figure 10. 3*d*-to-4*f* RIXS map of UO_2 with the incident energy on the *x*-axis and the (a) energy transfer or (b) emitted energy on the *y*-axis. The incident energy varies across the U M_4 edge. (c) Comparison between the calculated conventional XAS spectrum (black curve) at the U M_4 edge with a reduced core−hole lifetime broadening and a HERFD cut (red curve) of the 3*d*-to-4*f* RIXS map along the incidence energy axis at an emitted energy corresponding to the RIXS maximum. This cut is indicated by a dashed line in panel (b). The spectra in panel (c) are normalized to a main maximum.

and HERFD is observed when the HERFD spectra are lacking some intensity on the low-incident-energy side of the main line and show the extra intensity on the high-incident-energy side, compared to conventional XAS spectral shapes. This becomes especially pronounced for CmO_2 (see Figure 6). A lack of some intensity on the low-energy side can be understood from the considerations similar to those described in ref 28. The high-spin states of the $3d^9 5f^{n+1}$ multiplet at the An M_5 edge have a tendency to be at a lower energy than the low-spin states. Such high-spin states have a tendency to elastically scatter/decay to states at the low energy transfer, so that the inelastic scattering weight is minimized. This is, in a way, similar to an observation of the relatively lower intensity on the low-energy side of the fluorescence-yield spectra as compared to XAS (see ref 9). On the other hand, the low-spin states have a tendency to scatter inelastically.

The origin of the extra intensity on the high-incident-energy side of the main line in the HERFD spectra can be understood from the analysis of the ThO_2 spectra (Figure 1), as an example. In the calculated conventional Th M_5 XAS spectrum of ThO_2, the XAS transition to the highest state of the $3d^9 5f^1$ multiplet is observed at 3341.5 eV and contributes to the main XAS peak, while the calculated Th M_5 HERFD spectrum shows, in addition, some structure at ∼3343.0 eV. An inspection of Figure 17 can explain the appearance of this structure. The figure includes two 3*d*-4*f* RIXS spectra calculated at incident energies of 3341.5

https://dx.doi.org/10.1021/acs.inorgchem.0c02032
Inorg. Chem. 2020, 59, 16251−16264

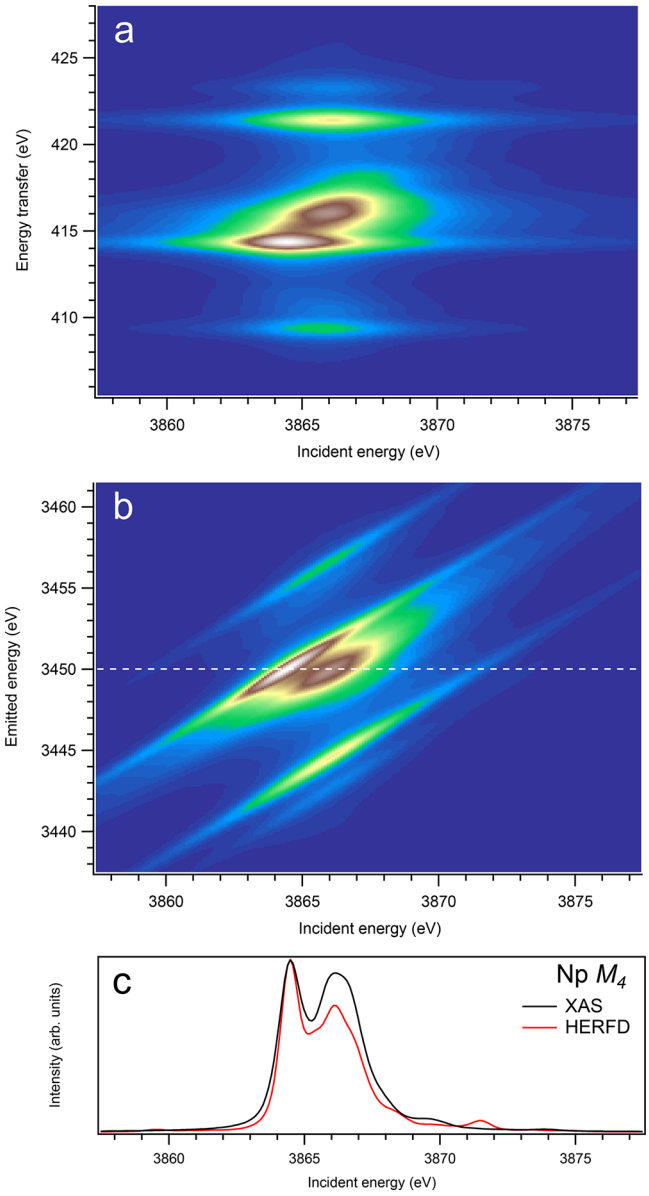

Figure 11. 3*d*-to-4*f* RIXS map of NpO_2 with the incident energy on the *x*-axis and the (a) energy transfer or (b) emitted energy on the *y*-axis. The incident energy varies across the Np M_4 edge. (c) Comparison between the calculated conventional XAS spectrum (black curve) at the Np M_4 edge with a reduced core−hole lifetime broadening and a HERFD cut (red curve) of the 3*d*-to-4*f* RIXS map along the incidence energy axis at an emitted energy corresponding to the RIXS maximum. This cut is indicated by a dashed line in panel (b). The spectra in panel (c) are normalized to a main maximum.

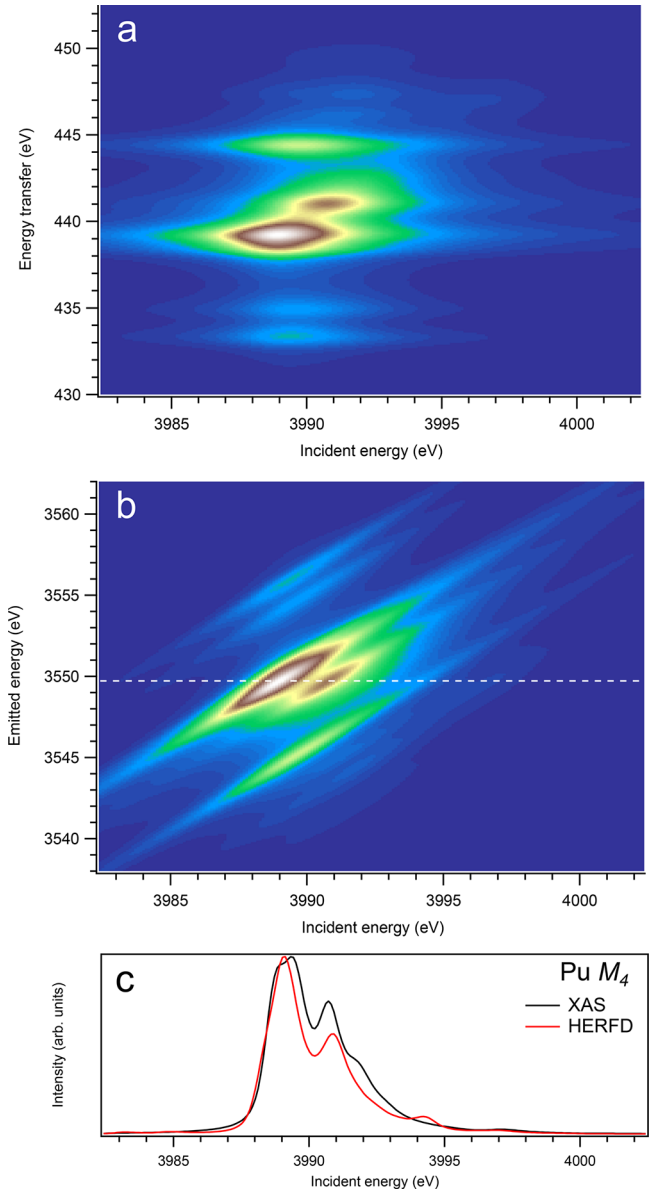

Figure 12. 3*d*-to-4*f* RIXS map of PuO_2 with the incident energy on the *x*-axis and the (a) energy transfer or (b) emitted energy on the *y*-axis. The incident energy varies across the Pu M_4 edge. (c) Comparison between the calculated conventional XAS spectrum (black curve) at the Pu M_4 edge with a reduced core−hole lifetime broadening and a HERFD cut (red curve) of the 3*d*-to-4*f* RIXS map along the incidence energy axis at an emitted energy corresponding to the RIXS maximum. This cut is indicated by a dashed line in panel (b). The spectra in panel (c) are normalized to a main maximum.

and 3343.0 eV (spectra A and B, respectively), which are displayed on the emitted energy scale. The spectra represent transitions to the states of the $4f^{13}5f^{1}$ multiplet. Since the vertical line in Figure 17 corresponds the emitted energy of the M_5 HERFD cut in Figure 1, one can see that spectrum B still has a significant intensity at this emitted energy when the incident energy is at 3343.0 eV. That is because the states of the $4f^{13}5f^{1}$ multiplet show a wider spread in energy than the states of the $3d^{9}5f^{1}$ multiplet, because of larger $F^{2,4,6}(4f,5f)$ and $G^{2,4,6}(4f,5f)$ integrals, thus still offering the possibility for the excited state to decay by emitting a photon with the energy used for the detection of the HERFD spectrum. Therefore, the ∼3343.0 eV structure in the calculated Th M_5 HERFD spectrum of ThO_2 (Figure 1) can be considered as the final state effect of the 3*d*-4*f* RIXS process.

Overall, one can say that profiles of the An M_5 HERFD spectra do not follow the X-ray absorption cross-section at the An M_5 edges of An dioxides well and exhibit some extra structures, which are absent for the dipole transitions from the ground state to the states of the $3d^{9}5f^{n+1}$ multiplet. Furthermore, the Cf M_5 HERFD spectrum of CfO_2 was found to be very different from the Cf M_5 XAS spectrum. The cuts of the calculated An 3*d*-4*f* RIXS maps for the M_5 edge at several different emitted-photon energies were also checked, but they reveal no improvement in agreement with the calculated XAS spectra. Nevertheless, for most actinides, the M_5 HERFD spectra can be used for studies of

https://dx.doi.org/10.1021/acs.inorgchem.0c02032
Inorg. Chem. 2020, 59, 16251−16264

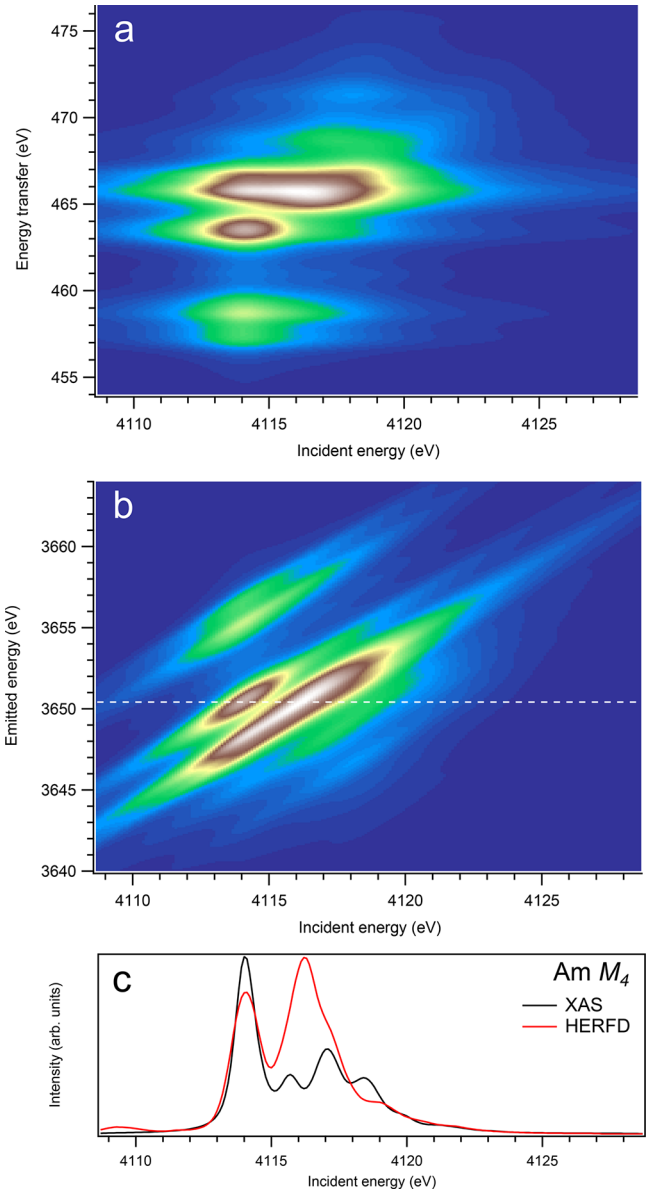

Figure 13. 3*d*-to-4*f* RIXS map of AmO_2 with the incident energy on the *x*-axis and the (a) energy transfer or (b) emitted energy on the *y*-axis. The incident energy varies across the Am M_4 edge. (c) Comparison between the calculated conventional XAS spectrum (black curve) at the Am M_4 edge with a reduced core−hole lifetime broadening and a HERFD cut (red curve) of the 3*d*-to-4*f* RIXS map along the incidence energy axis at an emitted energy corresponding to the RIXS maximum. This cut is indicated by a dashed line in panel (b). The spectra in panel (c) are normalized to a main maximum.

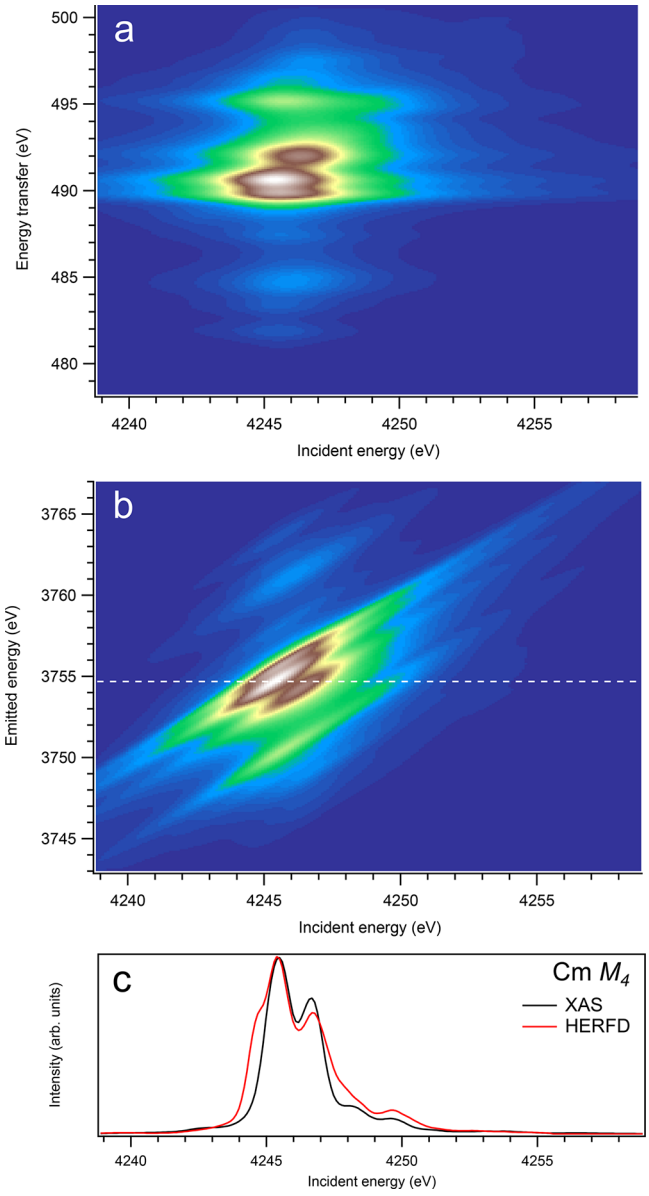

Figure 14. 3*d*-to-4*f* RIXS map of CmO_2 with the incident energy on the *x*-axis and the (a) energy transfer or (b) emitted energy on the *y*-axis. The incident energy varies across the Cm M_4 edge. (c) Comparison between the calculated conventional XAS spectrum (black curve) at the Cm M_4 edge with a reduced core−hole lifetime broadening and a HERFD cut (red curve) of the 3*d*-to-4*f* RIXS map along the incidence energy axis at an emitted energy corresponding to the RIXS maximum. This cut is indicated by a dashed line in panel (b). The spectra in panel (c) are normalized to a main maximum.

small variations in the chemical state (e.g., because of covalency), because the main maxima of the HERFD and XAS spectra coincide rather well (for UO_2, noticeable shift of ∼0.3 eV is found between HERFD and XAS maxima), regardless of the CfO_2 case.

On the other hand, at the An M_4 edges of dioxides (Figures 9−16), the calculated HERFD spectra reproduce the main structures of the XAS spectra (except for AmO_2), although the relative intensities of these structures vary between HERFD and XAS spectra for some dioxides. In particular, the main peak at ∼3742.5 eV in the U M_4 HERFD spectrum of UO_2 (Figure 10) is much stronger than other structures, while it is not the case for the U M_4 XAS spectrum. Nevertheless, the results of calculations for the An M_4 edges demonstrate overall better agreement between the HERFD and XAS spectra than that for the An M_5 edges. At the M_4 edge, the contribution of the states of the $3d^9 5f^{n+1}$ multiplet (which are the intermediate states in the 3*d*-4*f* RIXS process) to the XAS spectrum is more rich, in terms of observable structures, and is spread over a larger energy range, compared to that at the M_5 edge. Therefore, the final state effects due to the $4f^{13}5f^{n+1}$ multiplet involvement are less pronounced at the M_4 edge in the HERFD-XAS spectra (except for the significantly separated-in-energy, weak structures appearing quite a few eV below and above of the main RIXS intensity maximum, which were discussed above). Furthermore, the high- and low-spin states of the $3d^9 5f^{n+1}$ multiplet are more intermixed in energy at the M_4 edge, compared to those at the M_5 edge,

https://dx.doi.org/10.1021/acs.inorgchem.0c02032
Inorg. Chem. 2020, 59, 16251−16264

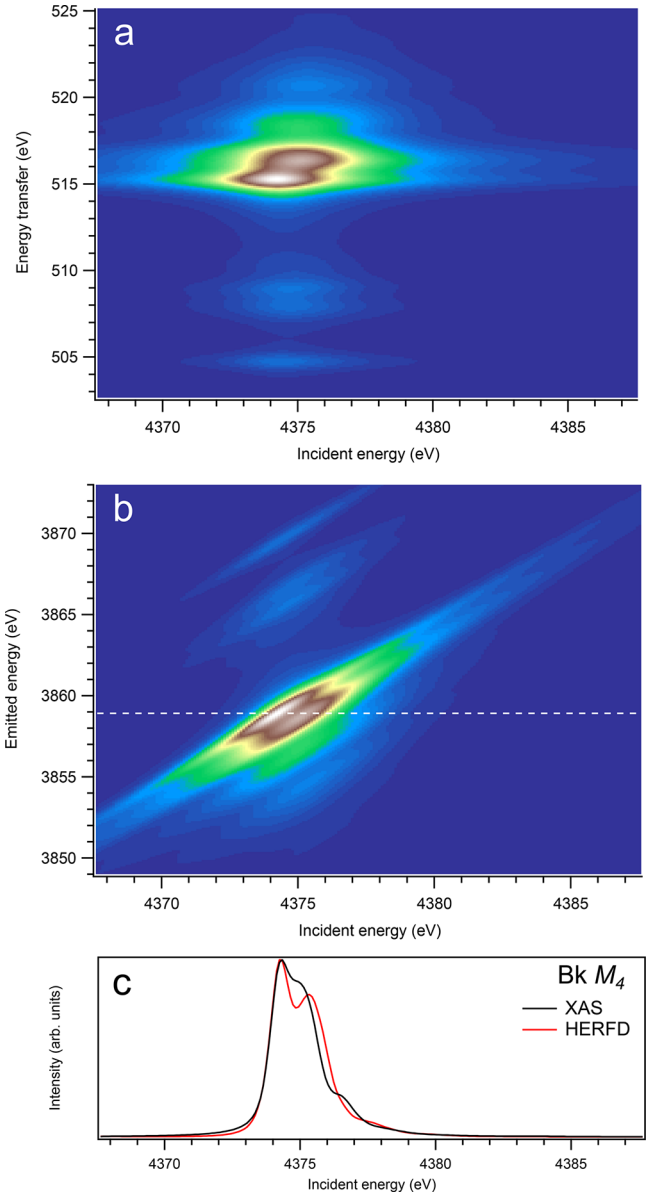

Figure 15. 3*d*-to-4*f* RIXS map of BkO_2 with the incident energy on the *x*-axis and the (a) energy transfer or (b) emitted energy on the *y*-axis. The incident energy varies across the Bk M_4 edge. (c) Comparison between the calculated conventional XAS spectrum (black curve) at the Bk M_4 edge with a reduced core−hole lifetime broadening and a HERFD cut (red curve) of the 3*d*-to-4*f* RIXS map along the incidence energy axis at an emitted energy corresponding to the RIXS maximum. This cut is indicated by a dashed line in panel (b). The spectra in panel (c) are normalized to a main maximum.

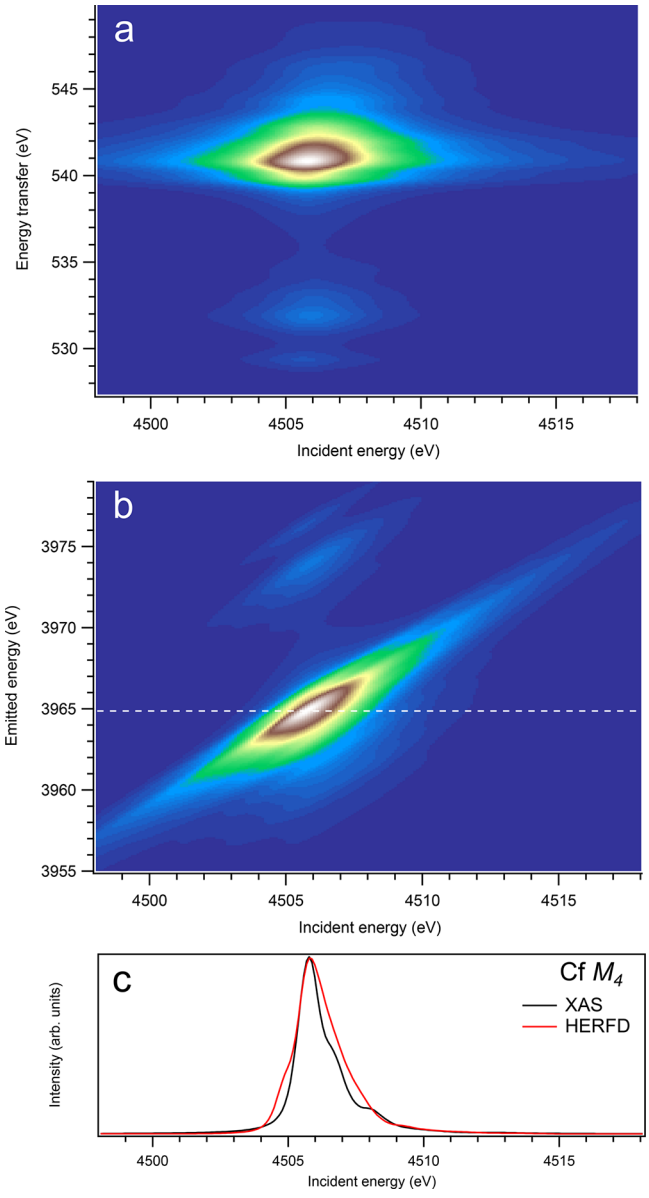

Figure 16. 3*d*-to-4*f* RIXS map of CfO_2 with the incident energy on the *x*-axis and the (a) energy transfer or (b) emitted energy on the *y*-axis. The incident energy varies across the Cf M_4 edge. (c) Comparison between the calculated conventional XAS spectrum (black curve) at the Cf M_4 edge with a reduced core−hole lifetime broadening and a HERFD cut (red curve) of the 3*d*-to-4*f* RIXS map along the incidence energy axis at an emitted energy corresponding to the RIXS maximum. This cut is indicated by a dashed line in panel (b). The spectra in panel (c) are normalized to a main maximum.

where high-spin states have a tendency to group on the low-energy side. In addition, the high-spin states are even preferentially distributed to the $3d_{5/2}$ manifold, compared to the $3d_{3/2}$ manifold.

XAS for the π-polarized incident beam was also calculated, since such polarization was used in RIXS calculations. A large difference between π-polarized and isotropic XAS spectra was found only at the Cf M_5 edge of CfO_2 (see the graphical Table of Contents entry). Some visible changes were found for U M_4, Np M_4 and Bk M_5 and M_4 XAS spectra. The structures at ∼3743.6 eV and ∼3866.3 eV in the π-polarized U M_4 and Np M_4 XAS spectra of UO_2 and NpO_2, respectively, somewhat grow up, as compared to the isotropic XAS spectra, thus making the agreement with the corresponding HERFD spectra worse. On the other hand, the structure at ∼4375.2 eV in the π-polarized Bk M_4 somewhat decreases, becomes more separated from the main peak and appears similar, shape-wise, to the corresponding (∼4375.3 eV) structure in the HERFD spectrum, thus improving an agreement with the HERFD spectrum, compared to the isotropic XAS spectrum. For other An M_5 and M_4 edges of An dioxides, negligible or no changes were found between the calculated π-polarized and isotropic XAS spectra.

The incident and emitted energy scales shown in all figures use the ab initio Hartree−Fock values obtained in the calculations. For comparison with experimental spectra, some uniform shifts in energy will be required since these Hartree−Fock

https://dx.doi.org/10.1021/acs.inorgchem.0c02032
Inorg. Chem. 2020, 59, 16251−16264

Table 5. Calculated Ground State of Each An Dioxide[a]

	ground state
Th(IV)	Γ_1
U(IV)	Γ_4
Np(IV)	Γ_5
Pu(IV)	Γ_1
Am(IV)	Γ_7
Cm(IV)	Γ_1
Bk(IV)	Γ_5
Cf(IV)	Γ_2

[a]Since the finite exchange field is applied along the *z*-axis, the notation is for C_{4h} symmetry.

calculations were performed for actinide ions and do not take into account all the solid-state effects. Considering the available experimental data, recorded with high resolution, we find a fairly good agreement in the spectral shape between calculated and measured HERFD spectra for the Th M_4 edge of ThO_2,[3] for the U M_5 and M_4 edges of UO_2,[29] and for Np M_5 edge of NpO_2.[30] However, all of the main structures of the experimental Pu M_5 and M_4 HERFD spectra of PuO_2[5] are reproduced by the crystal-field multiplet calculations; the agreement between calculated and measured spectra becomes somewhat worse than that observed for dioxides of other early actinides. That is because, for PuO_2, AmO_2, CmO_2, BkO_2, and CfO_2, the An 5*f*-O 2*p*

Table 6. Energies of Calculated Lowest 50 States of the Ground-State Configuration

	Energy of Calculated Lowest 50 States (eV)						
	U(IV)	Np(IV)	Pu(IV)	Am(IV)	Cm(IV)	Bk(IV)	Cf(IV)
1	0	0	0	0	0	0	0
2	0.000437	0.000116	0.140209	0.000005	0.540210	0.002403	0.000690
3	0.000874	0.000869	0.140427	0.043055	0.540711	0.003639	0.006637
4	0.162052	0.000976	0.140628	0.043840	0.541201	0.003895	0.007403
5	0.162059	0.050629	0.281582	0.044352	0.941752	0.004333	0.007659
6	0.186396	0.050801	0.282453	0.045177	0.942714	0.006920	0.029101
7	0.186404	0.051268	0.283337	0.573034	0.943685	0.009664	0.068869
8	0.186433	0.051448	0.337378	0.573518	1.110897	0.012176	0.069718
9	0.201998	0.216236	0.337380	0.585869	1.110900	2.143442	0.070097
10	0.712436	0.217063	0.817785	0.586352	1.377968	2.144058	0.079095
11	0.712689	0.785632	0.817819	0.657296	1.378088	2.165868	0.079509
12	0.712947	0.785647	0.817851	0.657737	1.378172	2.166272	0.079816
13	0.764943	0.785703	0.894213	0.657968	1.414808	2.166475	0.086039
14	0.764946	0.785717	0.894234	0.658410	1.415237	2.166903	0.563345
15	0.866262	0.793086	0.909607	1.022706	1.415767	2.359622	0.564439
16	0.866292	0.793286	0.909755	1.022806	1.465954	2.360696	0.565559
17	0.866323	0.805680	0.909862	1.029538	1.539842	2.778381	0.610518
18	0.932381	0.806050	0.959631	1.030273	1.685109	2.779099	0.610559
19	0.932381	0.937444	0.960114	1.030450	1.685745	2.779881	0.676096
20	0.981504	0.937488	0.960596	1.031202	1.686419	2.780584	0.676307
21	0.981528	0.937515	1.319922	1.090889	1.757103	2.836505	0.676468
22	0.981551	0.937559	1.355774	1.091158	1.757141	2.837790	0.791793
23	1.088487	1.367596	1.355909	1.091520	1.800204	2.918306	0.813146
24	1.088545	1.367696	1.356042	1.091792	1.801407	2.918612	0.813789
25	1.088604	1.367889	1.387479	1.161742	1.802600	2.935070	0.815038
26	1.282620	1.367991	1.387608	1.161861	1.862377	2.935195	0.823320
27	1.282766	1.411611	1.387725	1.188532	1.863499	2.935286	0.823629
28	1.282919	1.411710	1.402413	1.188922	1.864563	2.935415	0.913698
29	1.333085	1.421815	1.402422	1.189253	1.907768	3.021161	0.914963
30	1.373473	1.422187	1.402462	1.189654	1.909179	3.021440	0.915984
31	1.373662	1.459308	1.422079	1.219939	1.910628	3.049033	0.925494
32	1.373854	1.459380	1.497653	1.220114	1.975964	3.049202	0.926425
33	1.377929	1.459639	1.497654	1.221170	2.017553	3.077609	0.927584
34	1.378031	1.459709	1.702734	1.221357	2.018235	3.077715	1.190593
35	1.378148	1.573486	1.702737	1.342689	2.022628	3.077739	1.191101
36	1.389335	1.573876	1.702741	1.343907	2.023032	3.077851	1.192890
37	1.389337	1.602028	1.730997	1.495170	2.023501	3.146640	1.194162
38	1.442094	1.602353	1.730999	1.495303	2.059061	3.147621	1.194576
39	1.563278	1.602451	1.733273	1.498921	2.086984	3.147907	1.209760
40	1.563475	1.602786	1.765206	1.499036	2.088230	3.148882	1.276036
41	1.563672	1.696178	1.765749	1.499445	2.089167	3.221727	1.276489
42	1.618824	1.696210	1.766284	1.499537	2.089634	3.221791	1.276865
43	1.619216	1.696340	1.808581	1.526819	2.090567	3.222110	1.430133
44	1.619610	1.696374	1.808999	1.527237	2.090696	3.222187	1.431244
45	1.654628	1.701717	1.809266	1.527761	2.091425	3.324495	1.432351

https://dx.doi.org/10.1021/acs.inorgchem.0c02032
Inorg. Chem. 2020, 59, 16251−16264

Table 6. continued

	Energy of Calculated Lowest 50 States (eV)						
	U(IV)	Np(IV)	Pu(IV)	Am(IV)	Cm(IV)	Bk(IV)	Cf(IV)
46	1.695464	1.701739	1.810614	1.528133	2.108428	3.325577	1.619385
47	1.695482	1.726803	1.810623	1.548001	2.108584	3.337795	1.628049
48	1.695498	1.726868	1.810764	1.548928	2.121231	3.337800	1.628741
49	1.764655	1.726951	1.816994	1.622409	2.122550	3.338883	1.628862
50	1.764659	1.727015	1.816997	1.622917	2.123524	3.339027	1.977611

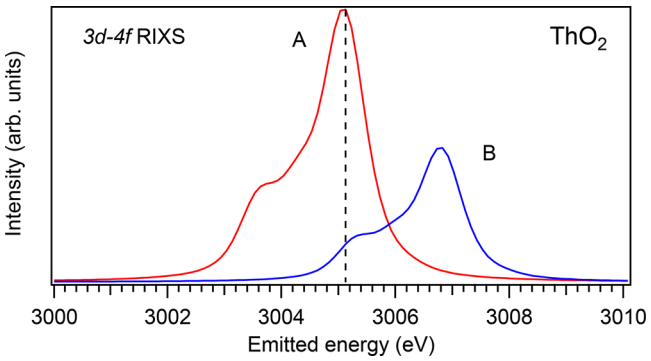

Figure 17. Two 3*d*-4*f* RIXS spectra of ThO_2 calculated for incident energies of 3341.5 (curve A) and 3343.0 eV (curve B).

charge-transfer effects become significant and must be taken into account in calculations of X-ray spectroscopic data.[31] Furthermore, the calculations of the Slater integrals specifically for compounds in question, using, e.g., the density functional theory approach instead of using the scaled atomic values of the Slater integrals for actinide ions, should improve the agreement between RIXS/HERFD calculations and the experiment. Note that the Am dioxide is claimed[32] to be hypostoichiometric without high oxygen pressure, which makes it difficult to perform a comparison using the results of present calculations.

SUMMARY

The results of crystal-field multiplet calculations of 3*d*-4*f* RIXS of An dioxides indicate that the 3*d*-4*f* RIXS profiles significantly differ for the An M_5 and M_4 edges. Both of the selection rules, when the $4f_{7/2}$ and $4f_{5/2}$ components are involved in the $5f^n \rightarrow 3d^9 5f^{n+1} \rightarrow 4f^{13} 5f^{n+1}$ excitation−de-excitation process at the M_5 edge, whereas only the $4f_{5/2}$ component is involved at the M_4 edge, and the final state effects of the RIXS process due to the 4*f*-5*f* interaction are contributing to the calculated differences.

The simulation of the HERFD spectra by making cuts across the 3*d*-4*f* RIXS maps along the incident energy axis at the emitted energy, corresponding to the maximum of the RIXS intensity, shows that the HERFD technique at the An $M_{4,5}$ edges is indeed an efficient tool for the evaluation of the An chemical state. However, it was found that the An M_5 HERFD profiles are departing from the X-ray absorption cross-section, in terms of the existence of additional transitions, whereas the results of calculations for the An M_4 edges reveal overall better agreement between the HERFD and XAS spectra for most dioxides, keeping in mind the restricted HERFD resolution that is due to the core−hole lifetime broadening in the final state. Since the shape of the spectra is affected by both the An valency and the local symmetry at the An sites, our results indicate that, in some instances, it will be crucial to calculate the entire 3*d*-4*f* RIXS process in order to interpret the HERFD spectra.

AUTHOR INFORMATION

Corresponding Author

Sergei M. Butorin − *Molecular and Condensed Matter Physics, Department of Physics and Astronomy, Uppsala University, SE-751 20 Uppsala, Sweden;* orcid.org/0000-0003-3242-5305; Email: sergei.butorin@physics.uu.se

Complete contact information is available at: https://pubs.acs.org/10.1021/acs.inorgchem.0c02032

Notes

The author declares no competing financial interest.

ACKNOWLEDGMENTS

The author acknowledges support from the Swedish Research Council (Research Grant No. 2017-06465).

REFERENCES

(1) Kvashnina, K. O.; Butorin, S. M.; Martin, P.; Glatzel, P. Chemical State of Complex Uranium Oxides. *Phys. Rev. Lett.* **2013**, *111*, 253002.

(2) Vitova, T.; Denecke, M. A.; Göttlicher, J.; Jorissen, K.; Kas, J. J.; Kvashnina, K.; Prüßmann, T.; Rehr, J. J.; Rothe, J. Actinide and lanthanide speciation with high-energy resolution X-ray techniques. *J. Phys.: Conf. Ser.* **2013**, *430*, No. 012117.

(3) Butorin, S. M.; Kvashnina, K. O.; Vegelius, J. R.; Meyer, D.; Shuh, D. K. High-resolution X-ray absorption spectroscopy as a probe of crystal-field and covalency effects in actinide compounds. *Proc. Natl. Acad. Sci. U. S. A.* **2016**, *113*, 8093−8097. Note that, because of the erroneous offset in energy, the RIXS map at the M_5 edge instead of the M_4 edge was used in Figure 2A of this reference. Therefore, the calculated XAS spectrum at the M_4 edge in Figure 2B of this reference is erroneously compared with the HERFD-XAS cut of the RIXS map calculated at the M_5 edge. The error does not affect the main conclusions of this reference, since they are based on the comparison of experimental data with calculations of XAS (not HERFD) spectra.

(4) Butorin, S. M.; Kvashnina, K. O.; Prieur, D.; Rivenet, M.; Martin, P. M. Characteristics of chemical bonding of pentavalent uranium in La-doped UO_2. *Chem. Commun.* **2017**, *53*, 115−118.

(5) Kvashnina, K. O.; Romanchuk, A. Y.; Pidchenko, I.; Amidani, L.; Gerber, E.; Trigub, A.; Rossberg, A.; Weiss, S.; Popa, K.; Walter, O.; Caciuffo, R.; Scheinost, A. C.; Butorin, S. M.; Kalmykov, S. N. A Novel Metastable Pentavalent Plutonium Solid Phase on the Pathway from Aqueous Plutonium(VI) to PuO_2 Nanoparticles. *Angew. Chem., Int. Ed.* **2019**, *58*, 17558−17562.

(6) Butorin, S. M.; Kvashnina, K. O.; Smith, A. L.; Popa, K.; Martin, P. M. Crystal-Field and Covalency Effects in Uranates: An X-ray Spectroscopic Study. *Chem. - Eur. J.* **2016**, *22*, 9693−9698.

(7) Butorin, S. M.; Modin, A.; Vegelius, J. R.; Kvashnina, K. O.; Shuh, D. K. Probing Chemical Bonding in Uranium Dioxide by Means of High-Resolution X-ray Absorption Spectroscopy. *J. Phys. Chem. C* **2016**, *120*, 29397−29404.

(8) Tanaka, S.; Okada, K.; Kotani, A. Resonant X-Ray Emission Spectroscopy in Dy Compounds. *J. Phys. Soc. Jpn.* **1994**, *63*, 2780−2787.

(9) Kurian, R.; Kunnus, K.; Wernet, P.; Butorin, S. M.; Glatzel, P.; de Groot, F. M. F. Intrinsic deviations in fluorescence yield detected x-ray

https://dx.doi.org/10.1021/acs.inorgchem.0c02032
Inorg. Chem. 2020, 59, 16251−16264

absorption spectroscopy: the case of the transition metal $L_{2,3}$ edges. *J. Phys.: Condens. Matter* **2012**, *24*, 452201.
(10) Lynch, D. W.; Cowan, R. D. Effect of hybridization on $4d \rightarrow 4f$ spectra in light lanthanides. *Phys. Rev. B: Condens. Matter Mater. Phys.* **1987**, *36*, 9228−9233.
(11) Nakotte, H.; Rajaram, R.; Kern, S.; McQueeney, R. J.; Lander, G. H.; Robinson, R. A. Crystal fields in UO_2 - revisited. *J. Phys.: Conf. Ser.* **2010**, *251*, No. 012002.
(12) Amoretti, G.; Blaise, A.; Caciuffo, R.; Cola, D. D.; Fournier, J. M.; Hutchings, M. T.; Lander, G. H.; Osborn, R.; Severing, A.; Taylor, A. D. Neutron-scattering investigation of the electronic ground state of neptunium dioxide. *J. Phys.: Condens. Matter* **1992**, *4*, 3459−3478.
(13) Magnani, N.; Amoretti, G.; Carretta, S.; Santini, P.; Caciuffo, R. Unified crystal-field picture for actinide dioxides. *J. Phys. Chem. Solids* **2007**, *68*, 2020−2023.
(14) Kern, S.; Robinson, R. A.; Nakotte, H.; Lander, G. H.; Cort, B.; Watson, P.; Vigil, F. A. Crystal-field transition in PuO_2. *Phys. Rev. B: Condens. Matter Mater. Phys.* **1999**, *59*, 104−106.
(15) Hubert, S.; Thouvenot, P.; Edelstein, N. Spectroscopic studies and crystal-field analyses of Am3+ and Eu3+ in the cubic-symmetry site of ThO_2. *Phys. Rev. B: Condens. Matter Mater. Phys.* **1993**, *48*, 5751−5760.
(16) Thouvenot, P.; Hubert, S.; Edelstein, N. Spectroscopic study and crystal-field analysis of Cm3+ in the cubic-symmetry site of ThO_2. *Phys. Rev. B: Condens. Matter Mater. Phys.* **1994**, *50*, 9715−9720.
(17) Cowan, R. D. *The Theory of Atomic Structure and Spectra*; Los Alamos Series in Basic and Applied Sciences, Vol. 3; University of California Press: Berkeley, CA, 1981.
(18) Butler, P. H. *Point Group Symmetry Applications: Methods and Tables*; Plenum Press: New York, 1981.
(19) Thole, B.; Van Der Laan, G.; Butler, P. Spin-mixed ground state of Fe phthalocyanine and the temperature-dependent branching ratio in X-ray absorption spectroscopy. *Chem. Phys. Lett.* **1988**, *149*, 295−299.
(20) Campbell, J.; Papp, T. Width of the atomic K−N_7 levels. *At. Data Nucl. Data Tables* **2001**, *77*, 1−56.
(21) Ogasawara, H.; Kotani, A.; Thole, B. T. Calculation of magnetic x-ray dichroism in 4 *d* and 5 *d* absorption spectra of actinides. *Phys. Rev. B: Condens. Matter Mater. Phys.* **1991**, *44*, 2169−2181.
(22) Glatzel, P.; Bergmann, U.; Gu, W.; Wang, H.; Stepanov, S.; Mandimutsira, B. S.; Riordan, C. G.; Horwitz, C. P.; Collins, T.; Cramer, S. P. Electronic Structure of Ni Complexes by X-ray Resonance Raman Spectroscopy (Resonant Inelastic X-ray Scattering). *J. Am. Chem. Soc.* **2002**, *124*, 9668−9669.
(23) de Groot, F. M. F.; Glatzel, P.; Bergmann, U.; van Aken, P. A.; Barrea, R. A.; Klemme, S.; Havecker, M.; Knop-Gericke, A.; Heijboer, W. M.; Weckhuysen, B. M. 1s2p Resonant Inelastic X-ray Scattering of Iron Oxides. *J. Phys. Chem. B* **2005**, *109*, 20751−20762.
(24) Lundberg, M.; Kroll, T.; DeBeer, S.; Bergmann, U.; Wilson, S. A.; Glatzel, P.; Nordlund, D.; Hedman, B.; Hodgson, K. O.; Solomon, E. I. Metal−Ligand Covalency of Iron Complexes from High-Resolution Resonant Inelastic X-ray Scattering. *J. Am. Chem. Soc.* **2013**, *135*, 17121−17134.
(25) Butorin, S. M.; Modin, A.; Vegelius, J. R.; Suzuki, M.-T.; Oppeneer, P. M.; Andersson, D. A.; Shuh, D. K. Local Symmetry Effects in Actinide 4f X-ray Absorption in Oxides. *Anal. Chem.* **2016**, *88*, 4169−4173.
(26) Moser, H. R.; Delley, B.; Schneider, W. D.; Baer, Y. Characterization of f electrons in light lanthanide and actinide metals by electron-energy-loss and x-ray photoelectron spectroscopy. *Phys. Rev. B: Condens. Matter Mater. Phys.* **1984**, *29*, 2947−2955.
(27) Caciuffo, R.; van der Laan, G.; Simonelli, L.; Vitova, T.; Mazzoli, C.; Denecke, M. A.; Lander, G. H. Uranium 5d−5f electric-multipole transitions probed by nonresonant inelastic x-ray scattering. *Phys. Rev. B: Condens. Matter Mater. Phys.* **2010**, *81*, 195104.
(28) Thole, B. T.; van der Laan, G. Branching ratio in x-ray absorption spectroscopy. *Phys. Rev. B: Condens. Matter Mater. Phys.* **1988**, *38*, 3158−3171.
(29) Kvashnina, K.; Kvashnin, Y.; Butorin, S. Role of resonant inelastic X-ray scattering in high-resolution core-level spectroscopy of actinide materials. *J. Electron Spectrosc. Relat. Phenom.* **2014**, *194*, 27−36.
(30) Bahl, S. P. Advanced Chemical and Structural Characterization of Nuclear Waste Materials Related to the Nuclear Fuel Cycle. Ph.D. Thesis, Karlsruhe Institut für Technologie, Karlsruhe, Germany, 2017.
(31) Kotani, A.; Ogasawara, H. Theory of core-level spectroscopy in actinide systems. *Phys. B* **1993**, *186−188*, 16−20.
(32) Epifano, E.; Guéneau, C.; Belin, R. C.; Vauchy, R.; Lebreton, F.; Richaud, J.-C.; Joly, A.; Valot, C.; Martin, P. M. Insight into the Am−O Phase Equilibria: A Thermodynamic Study Coupling High-Temperature XRD and CALPHAD Modeling. *Inorg. Chem.* **2017**, *56*, 7416−7432.

https://dx.doi.org/10.1021/acs.inorgchem.0c02032
Inorg. Chem. 2020, 59, 16251−16264